A&A 639, A115 (2020)
https://doi.org/10.1051/0004-6361/202037733

Astronomy & Astrophysics

Interferometric imaging with LOFAR remote baselines of the fine structures of a solar type-IIIb radio burst⋆

PeiJin Zhang (张沛锦)[1,2,3,4], Pietro Zucca[4], Sarrvesh Seethapuram Sridhar[4], ChuanBing Wang (王传兵)[1,2,3], Mario M. Bisi[7], Bartosz Dabrowski[6], Andrzej Krankowski[6], Gottfried Mann[9], Jasmina Magdalenic[8], Diana E. Morosan[5], and Christian Vocks[9]

[1] CAS Key Laboratory of Geospace Environment, School of Earth and Space Sciences, University of Science and Technology of China, Hefei, Anhui 230026, PR China
e-mail: pjer1316@mail.ustc.edu.cn,cbwang@ustc.edu.cn
[2] CAS Center for the Excellence in Comparative Planetology, USTC, Hefei, Anhui 230026, PR China
[3] Anhui Mengcheng Geophysics National Observation and Research Station, USTC, Mengcheng, Anhui 233500, PR China
[4] ASTRON, The Netherlands Institute for Radio Astronomy, Oude Hoogeveensedijk 4, 7991 PD Dwingeloo, The Netherlands
e-mail: zucca@astron.nl
[5] Department of Physics, University of Helsinki, PO Box 64, 00014 Helsinki, Finland
[6] Space Radio-Diagnostics Research Centre, University of Warmia and Mazury in Olsztyn, Olsztyn, Poland
[7] RAL Space, United Kingdom Research and Innovation (UKRI) – Science and Technology Facilities Council (STFC) – Rutherford Appleton Laboratory (RAL), Harwell Campus, Oxfordshire OX11 0QX, UK
[8] Solar-Terrestrial Centre of ExcellenceSIDC, Royal Observatory of Belgium, 1180 Brussels, Belgium
[9] Leibniz-Institut für Astrophysik Potsdam, An der Sternwarte 16, 14482 Potsdam, Germany

Received 14 February 2020 / Accepted 16 May 2020

ABSTRACT

Context. Solar radio bursts originate mainly from high energy electrons accelerated in solar eruptions like solar flares, jets, and coronal mass ejections. A sub-category of solar radio bursts with short time duration may be used as a proxy to understand wave generation and propagation within the corona.
Aims. Complete case studies of the source size, position, and kinematics of short term bursts are very rare due to instrumental limitations. A comprehensive multi-frequency spectroscopic and imaging study was carried out of a clear example of a solar type IIIb-III pair.
Methods. In this work, the source of the radio burst was imaged with the interferometric mode, using the remote baselines of the LOw Frequency ARray (LOFAR). A detailed analysis of the fine structures in the spectrum and of the radio source motion with imaging was conducted.
Results. The study shows how the fundamental and harmonic components have a significantly different source motion. The apparent source of the fundamental emission at 26.56 MHz displaces away from the solar disk center at about four times the speed of light, while the apparent source of the harmonic emission at the same frequency shows a speed of <0.02 c. The source size of the harmonic emission observed in this case is smaller than that in previous studies, indicating the importance of the use of remote baselines.

Key words. Sun: radio radiation – Sun: activity – methods: observational

1. Introduction

Solar type III radio bursts are among the brightest solar radio bursts observed (e.g., Wild et al. 1963; Reid & Ratcliffe 2014). The major defining characteristic of type III radio bursts is their fast frequency drift rate, which is about 10 MHz s^{-1} in the decametre range (Melnik et al. 2011; Zhang et al. 2018). Type III bursts are generated by weakly relativistic electron beams moving through the coronal plasma along open magnetic field structures. It is generally believed that the electron beam can excite Langmuir waves at the local plasma frequency, which can be expressed as $f_{pe}[\mathrm{kHz}] \approx 8.98\sqrt{N_e[\mathrm{cm}^{-3}]}$; the Langmuir waves can than be converted into electromagnetic waves at the fundamental or harmonic frequency through non-linear processes (Ginzburg & Zhelezniakov 1958; Reid & Ratcliffe 2014). One alternative mechanism, namely electron cyclotron maser (ECM) emission, was also proposed for the excitation of type III bursts (Wu et al. 2002; Chen et al. 2017).

A number of type III bursts show a fundamental-harmonic (F-H) pair structure. A type IIIb-III pair is a special kind of type III F-H pair events, which are characterised by the presence of fine structures in the fundamental part (Dulk & Suzuki 1980; Melnik et al. 2018). The generation mechanism of the type IIIb resulting in these fine structures in the spectrum is still debated. Based on the ECM emission, the fine structures can be generated due to modulation of the wave excitation by low-frequency Magnetohydrodynamics waves (Wang 2015; Zhao et al. 2013). The commonly held belief about the plasma emission mechanism is that density inhomogeneities in the background plasma create a clumpy distribution of Langmuir waves and are the cause of type IIIb fine structures (Takakura & Yousef 1975; Kontar 2001; Loi et al. 2014). Mugundhan et al. (2017) used the flux intensity variation at different frequencies to estimate the amplitude and scale of the density fluctuations. Most of the previous type IIIb burst studies focused on the dynamic spectrum.

Imaging of the type IIIb source can help in understanding the generation and propagation of the radio wave.

⋆ Movie associated to Fig. 2 is available at https://www.aanda.org

Abranin et al. (1976) used the Ukrainian T-shaped Radio telescope (UTR) operated as a one-dimensional heliograph to study the angular size of the type IIIb-III pair events. They studied the source size at 25 MHz and 12.5 MHz, and found that there are no significant changes in the second harmonic part. The source size for the harmonic part is about 20 arcmin and <40 arcmin at 25 and 12.5 MHz, respectively. The source size can be smaller than 10 arcmin for the fundamental part at 25 MHz. Kontar et al. (2017) performed tied array imaging and spectroscopy with core baselines (3.5 km) of a type IIIb event with the beamformed mode of the LOw Frequency ARray (LOFAR; van Haarlem et al. 2013). The study showed that, at a given frequency along the burst striae, the speed of the apparent source of the fundamental part moves faster than the harmonic part, and the source size (or area) increasing rate of the fundamental part is significantly larger than the harmonic part. The study also indicated that the observed wave duration and positions are convoluted by the wave generation, the scattering, and the refraction of the wave during the propagation. Sharykin et al. (2018) used the LOFAR beamformed method and studied the source size and position along several striae. The result shows that the source position along each stria is moving away from the Sun's center, and the area of the source increases with time.

The short term narrow-bandwidth radio emission is believed to be generated from a small area, while the observed source can have a large size and moving speed. For a better comprehension of the factors that influence the visual source, we acquired high spatial resolution images for the fine structures in the radio emission.

In this work, for the first time, we image a type IIIb-III pair event with LOFAR interferometric observations from the core and remote stations. In Sect. 2, the observation mode, data reduction process, and dyanmic spectrum of this type IIIb-III pair are described briefly. In Sect. 3, different source properties of the fundamental and harmonic components are presented. Finally, we discuss our results and summarize our conclusions in Sect. 4.

2. Observations and data reduction

LOFAR is an advanced radio antenna array that operates in the 10–250 MHz frequency range. LOFAR consists of two types of antennas: the low band array (LBA) and the high band array (HBA), which are sensitive to the 10–90 MHz and the 110–250 MHz frequency ranges, respectively. LOFAR has 52 stations, 38 of which are located in the Netherlands, and 14 international stations in Germany, Poland, France, Sweden, Ireland, the UK, and Latvia. Of the 38 Dutch stations, 24 stations are densely packed and are referred to as the "core" stations. The remaining 14 "remote" stations are sparsely distributed across the northern Netherlands. The core and the remote stations provide excellent instantaneous *uv*-coverage to produce images at a high spatial resolution combined with good sensitivity to emissions on large angular scales. This makes LOFAR an excellent instrument to study a complex source like the Sun. In this work, we make use of data from only the Dutch stations. Owing to its flexible software backend, it can observe in different modes including standard interferometric imaging, tied-array beamforming, and real-time triggering on incoming station data streams.

We carried out simultaneous interferometric and beamformed observations of the Sun with the Dutch LOFAR array using its LBA on 13 April 2019 (project code: LT10_002). The core and the remote stations were used in the interferometric mode, while only the core stations were used to obtain the beamformed mode. In the interferometric mode, we used 60 non-

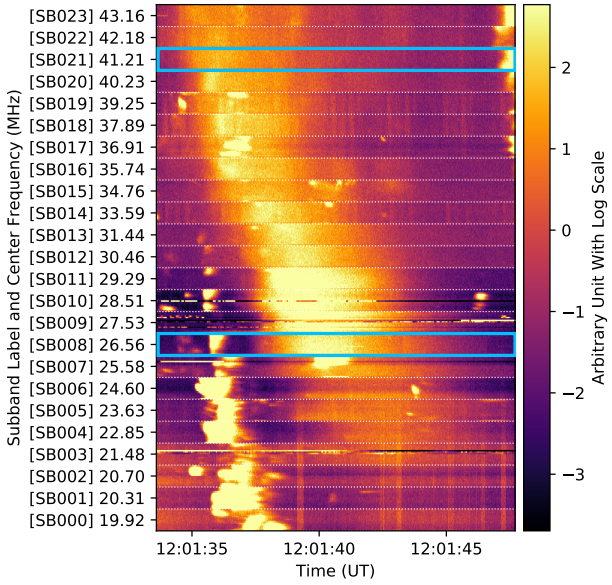

Fig. 1. Dynamic spectrum of the type IIIb-III pair event. The dynamic spectrum contains 24 subbands, the bandwidth of each subband is about 0.183 MHz. The frequency of this dynamic spectrum is not continuous. The blue box highlights the subband SB008 and SB021, which is used in the interferometric imaging.

contiguous subbands (SBs) to cover the 10–90 MHz frequency range. Each SB has a bandwidth of 195.3 kHz and is further subdivided into 16 channels resulting in a frequency resolution of 12.2 kHz. We recorded the visibility data with a correlator integration time of 0.167 s. Using the same observational setup, we also simultaneously observed Taurus A as a calibrator to derive the station gains. The projected baseline length for our observation is about 80 km, which results in a theoretical spatial resolution of about 36 arcsec. However, since we make images of the Sun with high temporal and frequency resolution, the achieved spatial resolution is higher due to the instantaneous *uv*-coverage and the applied visibility weighting.

We calibrated our correlated visibility data using the Default Pre-Processing Pipeline (DPPP; van Diepen et al. 2018). We derived the amplitude and the phase solutions using a model[1] for Taurus A and applied the derived gain solutions to the solar dataset. While deriving the gain solutions, we accounted for the difference in the station beam response toward the Sun and Taurus A. We imaged the calibrated visibilities using WSClean (Offringa et al. 2014; Offringa & Smirnov 2017) making use of it multiscale deconvolution algorithm. While imaging, we weighted the visibilities using the Briggs weighting scheme with the robust parameter set to 0.2 (Briggs 1995). We imaged and deconvolved visibility data from each 0.168 s separately, which allowed us to resolve the temporal variations in the Sun.

From our observations of the Sun, we identified the type IIIb-III event on 13 April 2019 at 12:01 UT (see Fig. 1). From Fig. 1 we can see that this is a typical type IIIb-III pair event. There is striae structure in the fundamental part. The frequency ratio of the harmonic and fundamental band is about 1.6. The upper frequency limit of the fundamental (type IIIb burst) part is about 30 MHz. We selected two SBs, with central frequencies 26.56 and 41.21 MHz, which are relatively free of other bursts. These SBs are indicated with blue boxes in Fig 1.

[1] https://github.com/lofar-astron/prefactor/blob/master/skymodels/Ateam_LBA_CC.skymodel

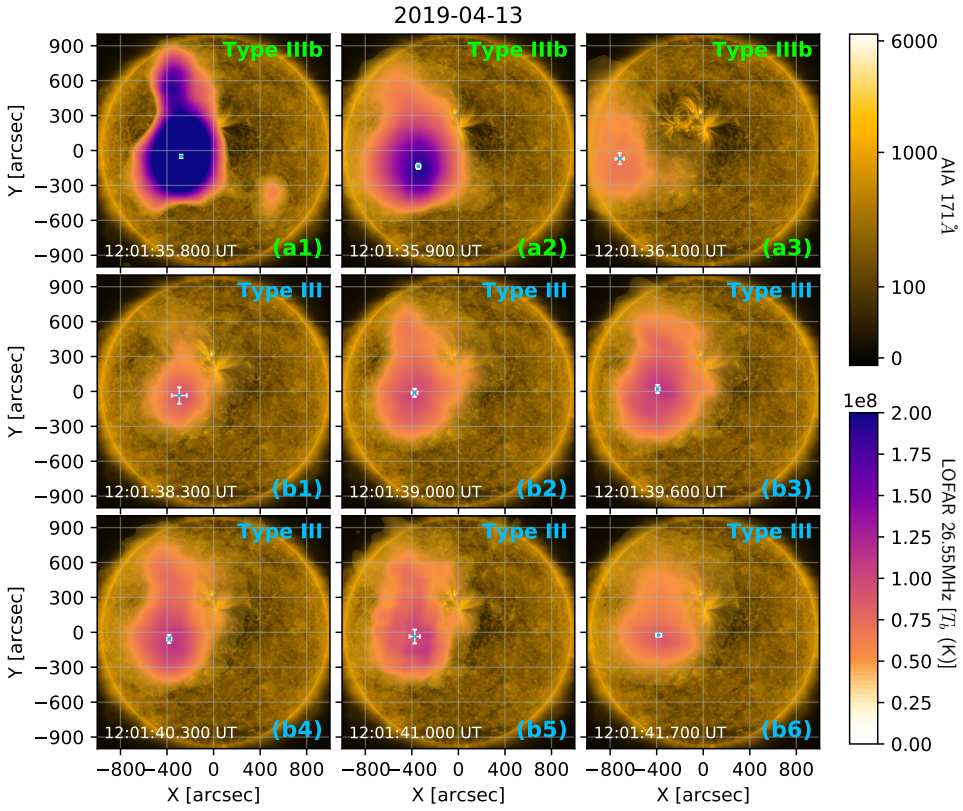

Fig. 2. Interferometry observation of the type IIIb-III pair. *Panel (a1–3)* is the interferometric image of the fundamental (type IIIb) part, and *Panel (b1–6)* shows the second harmonic (type III) part in subband SB008 (26.56 MHz). The radio flux intensity is overlaid on the EUV image observed by SDO/AIA at 12:01:33 UT. The unit of radio flux intensity in this is converted to brightness temperature (Kelvin). The times of snapshots are marked by vertical green or blue lines in the left-top sub-panel of Fig. 3. The peak position of the radio flux intensity is marked by a blue dot with position uncertainty marked as a white error bar in each snapshot. An animation of this figure is available online.

3. Results

Figure 2 shows the LOFAR interferometric imaging of the Sun at 26.56 MHz overlaid on the EUV image observed by the Atmospheric Imaging Assembly (AIA) on the Solar Dynamics Observatory (SDO) at 12:01:33 UT (Lemen et al. 2011). We see from Fig. 2 (a1-3) that, for the fundamental part, the apparent source moved about 500 arcsec within 0.3 s toward the limb. While for the harmonic part shown in Fig. 2(b1–6), the apparent source position is stable for the 3.4 s as shown in these six frames. At 26.56 MHz, the type IIIb source has a higher brightness temperature, and moves faster than the type III source. Fig. 2 also shows that, by employing long Dutch LOFAR baseline, we can resolve the source shape with unprecedented spatial resolution. The source shapes in Fig. 2(a1, a2) and (b2–4) are similar.

The brightness temperature was obtained from the flux intensity using the unit of [Jy/Beam] with $T_b = \lambda^2 S/(2k\Omega)$, where λ is the wavelength, k is the Boltzmann constant, S is the flux intensity, Ω is the solid angle of the beam. The uncertainty of the brightness temperature is determined by the standard deviation of the residual map. The source position and its uncertainty is obtained with the two-dimensional Gaussian fit method (Kontar et al. 2017; Zhang et al. 2019). The source area (A_s) is determined by the full width half maximum (FWHM) of the brightness temperature map. The uncertainty of the source area is determined as $\delta A_s = 2\sqrt{A_s(\delta x^2 + \delta y^2)}$, where δx and δy is the uncertainty of the source position. We did a survey on the source brightness, size, and movement for two SBs, namely 26.56 MHz and 41.21 MHz, shown in Fig. 3. The fundamental and harmonic parts both appear in 26.56 MHz (shown in the left panel of Fig. 3), the SB of 41.21M Hz only contains the harmonic part (shown in the right part of Fig. 3). The statistical and linear-fit results are shown in Table 1.

Figure 3 and Table 1 show the inteferometric analysis of the type IIIb-III event in 26.56 and 41.21 MHz with LOFAR core and remote stations. The flux peak time of the harmonic emission in 41.21 MHz is close to the peak time of the fundamental emission in 26.56 MHz. The main results of the imaging are as follows:

1. For the frequency SB of 26.56 MHz, the source area of the fundamental emission increases from about 50 arcmin^2 to 200 arcmin^2 within 0.45 s, while the source area of the fundamental is stable near about 100 arcmin^2 for the 6.61 seconds of duration.

2. For the frequency SB of 41.21 MHz, only harmonic emission is observed. The visual source area increases from about 50 arcmin^2 to 100 arcmin^2 in 5.31 s.

3. The visual speed of the source of fundamental emission at 26.56 MHz is about four times the speed of light.

4. The visual speed of the sources of harmonic emission at 26.56 MHz and 41.21 MHz are less than 0.11 times the speed of light.

There are significant differences between the source properties of the fundamental and harmonic waves. For the frequency SB of 26.56 MHz, the source area of the fundamental part increases fast, the increasing rate is 382 arcmin^2 per second starting from about 50 arcmin^2, while the increasing rate of the source area of the harmonic part is nearly zero for 26.56 MHz, and 8.7 arcmin^2 per second for 41.21 MHz. The speed of the apparent source is also widely divergent between the fundamental and harmonic parts. We need to note that, the speed of the apparent source is the visual speed of the brightest point in single frequency, not the physical position of the electron beams. The apparent source speed of the fundamental part is about 3.7 c for emissions at 26.56 MHz, while the source position of the harmonic part is stable, and the speed is about 0.015 c for 26.56 MHz and 0.11 c for 41.21 MHz.

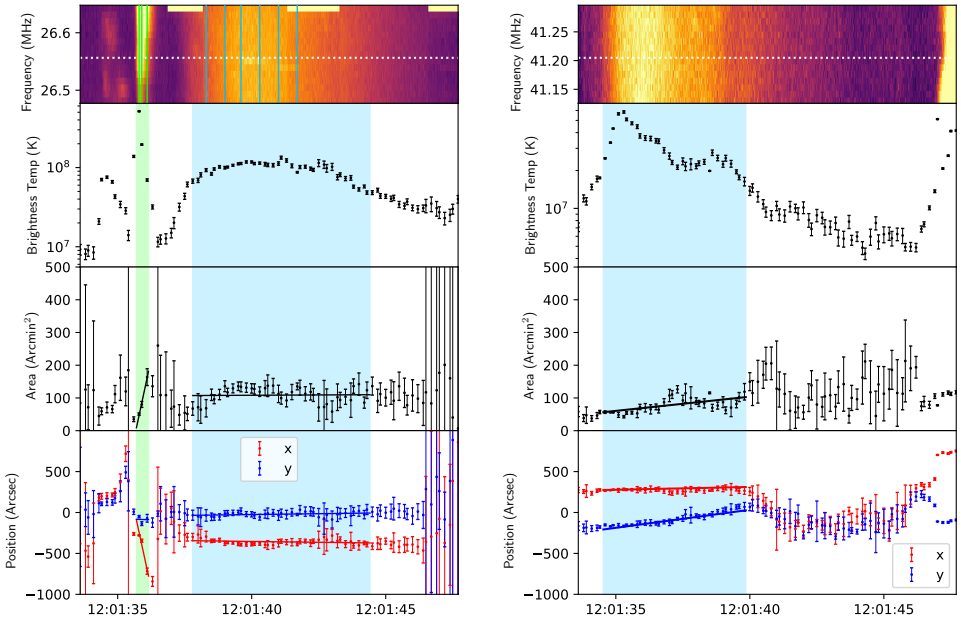

Fig. 3. Dynamic spectra of subband SB008 (*left*) and SB021 (*right*) with center frequencies of 26.56 MHz and 41.21 MHz (*top panel*), the source brightness temperature (*second panel*), and the size and position of these two subbands (*third and fourth panel*). The fundamental part is marked as green shadow, the harmonic part is marked as blue shadow, and the error bar marks the uncertainty.

Table 1. Full width half maximum duration, initial area, area increasing rate, and apparent velocity of the radio source in the two selected subbands.

	26.56 MHz (F)	26.56 MHz (H)	41.21 MHz (H)
t_{FWHM} [s]	0.45	6.61	5.31
A_0 [arcmin^2]	50.7 ± 3.7	67.7 ± 20.6	56.7 ± 3.8
dA/dt [arcmin^2 s^{-1}]	382 ± 30	0.4 ± 2.0	8.7 ± 2.1
v_x [c]	-3.67 ± 0.72	-0.010 ± 0.007	0.002 ± 0.004
v_y [c]	-0.03 ± 0.71	0.010 ± 0.006	0.115 ± 0.006

Notes. The velocity is in the unit of the speed of light. The second column show the results of the fundamental part of subband 26.56 MHz, the third and fourth column show the results of harmonic part of subbands 26.56 MHz and 41.21 MHz, respectively.

4. Discussion

The source size observed in this case is smaller than the results of previous studies. The FWHM area of the source is about 100 arcmin^2 for 26.56 and 41.21 MHz, with a minimal value of 50 arcmin^2. Abranin et al. (1976) measured the one-dimensional angular width of the type III radio burst source with UTR, and they obtained about 300 arcmin^2 for a source of 26 MHz. Kontar et al. (2017) used beamformed imaging from the LOFAR core station and analyzed the variation of the source size and position of the type IIIb-III pair, the source area is about 500 arcmin^2 for the fundamental and 700 arcmin^2 for the harmonic at 32.5 MHz. Sharykin et al. (2018) obtained about 350 arcmin^2 for the straie near 30.1 MHz with the LOFAR beamformed observation of type IIIb. The linearly fitted expansion rate of the fundamental wave in this case is 382 arcmin^2 s^{-1}, which is larger than previous results. Kontar et al. (2017) obtained the 180 arcmin^2 s^{-1} for fundamental, and 50 arcmin^2 s^{-1} for harmonic emission. Sharykin et al. (2018) measured the expansion rate along the straie of the type IIIb burst, the value of the expansion rate varies between 50 and 200 arcmin^2 s^{-1} during the burst.

The observed size and movement of the source is determined by both the original source property at the wave excitation site, namely the "real source" and the propagation effect of the radio waves. The type III radio burst is excited by the electron beam propagating outward along open magnetic field lines. The size and position of the real source at a given frequency f_s is determined by the wave excitation condition and the cross section of the electron beam at the altitude where the local plasma frequency satisfies $f_{pe} = f_s$ (or $f_s/2$ for harmonic) according to the plasma emission mechanism (Ginzburg & Zhelezniakov 1958; Reid & Ratcliffe 2014). The background conditions, namely the electron density and the magnetic fields are stable within the timescale of seconds. Consequently, the size and position of the real source should be stable at the generation site for the wave of f_s for short term bursts. However, the observation in this case shows that the observed source of the fundamental wave changed significantly. This indicates that the observed radio source is greatly influenced by the wave propagation effects, namely the wave refraction and the scattering. For these two factors, the variation of the source size is mainly dominated by the scattering effect. According to the simulation of anisotropic scattering (Kontar et al. 2019), the source FWHM width due to the scattering could be 1 solar radius at 32 MHz for fundamental waves with an anisotropy parameter of $\alpha = 0.3$ and a level of turbulence of $\epsilon = 0.8$.

The observed source expansion at a given frequency corresponds to the variation of the amount of scattering experienced by the waves. In this case, the source size of the fundamental emission increases from 50 arcmin^2 to 200 arcmin^2, which implies that the radio waves observed at the beginning of the type IIIb burst experience less scattering than those at the end of the type IIIb burst. Using the anisotropic simulation model by Kontar et al. (2019), we simulated the source expansion process for an ideal pulse point source of a fundamental emission at

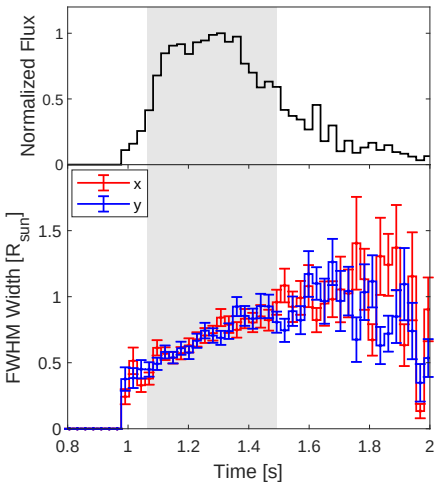

Fig. 4. Simulation result of the observed flux (*upper panel*) and the apparent source size (width) along the x and y axis (*lower panel*) for a impulse point source with frequency 26 MHz located at the solar disk center. In the simulation, we use a turbulence level of $\epsilon = 0.3$ and an isotropic parameter of $\alpha = 0.3$. The gray area represents the time range of the flux FWHM.

$f_s = 26$ MHz. The results are shown in Fig. 4. One can see that the source size increases during the time range of flux FWHM. In addition, the minimal observed source size can set a lower limit to the scattering effect. Using the LOFAR remote baseline for the imaging, the average fitted beam size is 180 arcsec (3 arcmin), which is also the resolution limit of this method. In this event, the minimal observed source size of fundamental emission is 50 arcmin^2 for the fundamental wave at $f_s = 26$ MHz, which requires $\epsilon = 0.3$ for the background according to the simulation result shown in Fig. 4. Statistical works that consider more type IIIb-III pair events analyzed with the interferometric of LOFAR remote baseline are needed to constrain the parameters related to the wave scattering.

Both the wave refraction and the scattering can contribute to the high speed visual movement of the source. In general, the refraction displaces the observed source position inward from its real location, and the scattering produces outward displacement of the apparent source. Ray-tracing simulation results show that, for an ideal point pulse source, the scattering and refraction of the waves will result in a visual motion of the source toward the solar center with time (Arzner & Magun 1999), though the transient position of the source is still been displaced outward from its real position. However, in this case, the observed source is moving outward from the solar disk center. This may be due to the simple assumptions used in the ray-tracing simulation, such as an ideal pulse point source, sphere symmetric distribution of the background density, and isotropic scattering. In fact, the corona is a highly non-uniform medium with a number of discrete large structures, including loops, coronal holes, helmet streamers, and bright and dark rays.

Some observations suggest that a type III burst may be generated in regions of enhanced density or along the streamers (Fainberg & Stone 1974). As a result, the radio waves will propagate away from the density-enhanced region after excitation, in an arbitrary direction depending on the observation view angle with respect to the streamer. On the other hand, Duncan (1979) and Calvert (1995) suggested that the wave of the radio burst can be guided by the under-dense flux tube. The escape point of the wave from the tube is determined by the density depletion factor, the wave frequency, and the wave angle (the angle between the wave vector and the magnetic field). For the event in this work, the harmonic component has a relatively stable apparent position and expands slowly. This indicates the ducting effect is weak for harmonic waves, or in other words the tube depletion factor is low. For the fundamental part, we expect that waves with a larger wave angle could escape earlier from the tube at a lower altitude than that of waves with a smaller wave angle from the same generation site. After the waves escape from the flux tube, the scattering will displace the wave source further outward . Moreover, the cross section of the tube increases with height due to the divergence of magnetic field, also producing an increase in the wave source size. This may explain the large expansion rate of the type IIIb source size, accompanied by the super-luminal source motion observed in this event. Ray-tracing simulations with photon scattering in different background environments may be helpful to clarify these in the future.

Acknowledgements. The analysis of the SDO/AIA data is done with Sunpy, and gnu Parallel is used for the acceleration of the imaging process. We are thankful to the ASTRON/JIVE Summer Student Programme 2019 for financial support. This paper is based on data obtained with the International LOFAR Telescope (ILT) under project code LT10 002. LOFAR (van Haarlem et al. 2013) is the LOw Frequency Array designed and constructed by ASTRON. It has observing, data processing, and data storage facilities in several countries, which are owned by various parties (each with their own funding sources), and that are collectively operated by the ILT foundation under a joint scientific policy. The ILT resources have benefited from the following recent major funding sources: CNRS-INSU, Observatoire de Paris and Universite Orleans, France; BMBF, MIWF-NRW, MPG, Germany; Science Foundation Ireland (SFI), Department of Business, Enterprise and Innovation (DBEI), Ireland; NWO, The Netherlands; The Science and Technology Facilities Council, UK; The Ministry of Science and Higher Education, Poland. The research in USTC was supported by the National Nature Science Foundation of China (41574167 and 41974199) and the B-type Strategic Priority Program of the Chinese Academy of Sciences (XDB41000000).

References

Abranin, E. P., Bazelian, L. L., Goncharov, N. I., et al. 1976, Sov. Astron., 19, 602
Arzner, K., & Magun, A. 1999, A&A, 351, 1165
Briggs, D. 1995, PhD thesis, New Mexico Institute of Mining and Technology
Calvert, W. 1995, J. Geophys. Res.: Space Phys., 100, 17491
Chen, L., Wu, D. J., Zhao, G. Q., & Tang, J. F. 2017, J. Geophys. Res. (Space Phys.), 122, 35
Dulk, G. A., & Suzuki, S. 1980, A&A, 88, 203
Duncan, R. 1979, Sol. Phys., 63, 389
Fainberg, J., & Stone, R. G. 1974, Space Sci. Rev., 16, 145
Ginzburg, V., & Zhelezniakov, V. 1958, Astron. Zh., 35, 694
Kontar, E. P. 2001, A&A, 375, 629
Kontar, E. P., Yu, S., Kuznetsov, A., et al. 2017, Nat. Commun., 8, 1515
Kontar, E. P., Chen, X., Chrysaphi, N., et al. 2019, ApJ, 884, 122
Lemen, J. R., Akin, D. J., Boerner, P. F., et al. 2011, The Solar Dynamics Observatory (Springer), 17
Loi, S. T., Cairns, I. H., & Li, B. 2014, ApJ, 790, 67
Melnik, V. N., Konovalenko, A. A., Rucker, H. O., et al. 2011, Sol. Phys., 269, 335
Melnik, V. N., Brazhenko, A. I., Frantsuzenko, A. V., Dorovskyy, V. V., & Rucker, H. O. 2018, Sol. Phys., 293,
Mugundhan, V., Hariharan, K., & Ramesh, R. 2017, Sol. Phys., 292,
Offringa, A. R., & Smirnov, O. 2017, MNRAS, 471, 301
Offringa, A., McKinley, B., Hurley-Walker, N., et al. 2014, MNRAS, 444, 606
Reid, H. A. S., & Ratcliffe, H. 2014, Res. Astron. Astrophys., 14, 773
Sharykin, I. N., Kontar, E. P., & Kuznetsov, A. A. 2018, Sol. Phys., 293, 115
Takakura, T., & Yousef, S. 1975, Sol. Phys., 40, 421
van Diepen, G., Dijkema, T.J., & Offringa, A. 2018, Astrophysics Source Code Library [record ascl:ascl.1804]
van Haarlem, M., Wise, M., Gunst, A., et al. 2013, A&A, 556, A2
Wang, C. B. 2015, ApJ, 806, 34
Wild, J., Smerd, S., & Weiss, A. 1963, ARA&A, 1, 291
Wu, C. S., Wang, C. B., Yoon, P. H., Zheng, H. N., & Wang, S. 2002, ApJ, 575, 1094
Zhang, P. J., Wang, C. B., & Ye, L. 2018, A&A, 618, A165
Zhang, P. J., Yu, S., Kontar, E. P., & Wang, C. B. 2019, ApJ, 885, 140
Zhao, G. Q., Chen, L., & Wu, D. J. 2013, ApJ, 779, 31